Time-resolved coherent anti-Stokes Raman scattering microscopy: Imaging based on Raman free induction decay

Andreas Volkmer, Lewis D. Book, and X. Sunney Xie

Articles you may be interested in

Improved contrast radially polarized coherent anti-Stokes Raman scattering microscopy using annular aperture detection
Appl. Phys. Lett. **95**, 133703 (2009); 10.1063/1.3240874

Vibrational dephasing time imaging by time-resolved broadband coherent anti-Stokes Raman scattering microscopy
Appl. Phys. Lett. **92**, 041108 (2008); 10.1063/1.2838750

Noncritical phase-matched lithium triborate optical parametric oscillator for high resolution coherent anti-Stokes Raman scattering spectroscopy and microscopy
Appl. Phys. Lett. **89**, 251116 (2006); 10.1063/1.2420773

Development of simultaneous frequency- and time-resolved coherent anti-Stokes Raman scattering for ultrafast detection of molecular Raman spectra
J. Chem. Phys. **125**, 044502 (2006); 10.1063/1.2219439

Coherent anti-Stokes Raman scattering microscopy with spectrally tailored ultrafast pulses
Rev. Sci. Instrum. **76**, 043108 (2005); 10.1063/1.1889471

Time-resolved coherent anti-Stokes Raman scattering microscopy: Imaging based on Raman free induction decay

Andreas Volkmer,[a] Lewis D. Book,[b] and X. Sunney Xie[c]

Harvard University, Department of Chemistry and Chemical Biology, 12 Oxford Street, Cambridge, Massachusetts 02138

A time-resolved coherent anti-Stokes Raman scattering (CARS) microscope allows three-dimensional imaging based on Raman free induction decay of molecular vibration with no requirement for labeling of the sample with natural or artificial fluorophores. A major benefit of the technique is the capability to completely remove nonresonant coherent background signal from the sample and the solvent, and thus increasing the detection sensitivity of CARS microscopy significantly. © *2002 American Institute of Physics.* [DOI: 10.1063/1.1456262]

Recent advances in nonlinear coherent microscopy, such as second-[1–3] and third-harmonic generation microscopy,[4,5] and coherent anti-Stokes Raman scattering (CARS) microscopy[6–9] have attracted much interest. Among coherent microscopies, CARS provides vibrational information intrinsic to and characteristic of chemical species. CARS is a third-order nonlinear optical process involving three laser beams (Fig. 1 inset), the pump, Stokes and probe beam with frequencies at ω_{P1}, ω_S, and ω_{P2}, respectively, which interact with the sample and generate an anti-Stokes field at a frequency $\omega_{AS} = \omega_{P1} + \omega_{P2} - \omega_S$ that is higher than the excitation frequencies. Therefore, CARS can be detected in the presence of one-photon induced fluorescence. The anti-Stokes signal is resonantly enhanced when the Raman shift, $\omega_{P1} - \omega_S$, coincides with the frequency of a Raman-active molecular vibration, which provides the intrinsic vibrational contrast mechanism.[10] Vibrational imaging based on CARS has been previously demonstrated to be more sensitive than infrared and confocal Raman microscopy techniques,[6] and has three-dimensional sectioning capability and deep penetration depth, similar to other nonlinear microscopy. Since the molecules remain in the electronic ground state, photobleaching and damage to delicate biological samples is minimized. However, CARS detection is not background free. Electronic contributions to the third-order susceptibility from the sample and solvent cause a nonresonant background signal, which provides no vibrational contrast. In addition, the solvent water has strong resonant signals of broad spectral width. Both background signals often overwhelm the CARS signal from small scatterers, and limit the sensitivity. Recently, we have reported significant advances in the sensitivity and spectral resolution of CARS microscopy and its application to the imaging of live unstained cells.[7–9]

Here we use time-resolved CARS (T-CARS)[11] to record the Raman free induction decay (RFID) of molecular vibrations. This not only provides spectroscopic information in the time domain, but also an alternative approach to separate the nonresonant contribution of RFID, which is instantaneous, from the resonant contribution of RFID[12] in CARS microscopy. The T-CARS experiment involves three incident electric fields, $\mathbf{E}_m(\mathbf{r},t)$, with frequencies at ω_m ($m = P1, P2$, and S) that induce a third-order nonlinear polarization, $\mathbf{P}^{(3)}(\mathbf{r},t)$ at ω_{AS}. Typically, the pair of the first pump pulse, $\mathbf{E}_{P1}(\mathbf{r},t)$, and the Stokes pulse, $\mathbf{E}_S(\mathbf{r},t)$, are temporally overlapped, and impulsively polarizes the sample. The third probe pulse, $\mathbf{E}_{P2}(\mathbf{r},t)$, then interacts with the sample at a certain delay time, τ, with respect to the previous pulse pair, and probes the relaxation of the induced polarization.

A detailed account on the spatial field distribution of tightly focused incident fields and the signal generation in CARS microscopy has been given elsewhere.[7,13] Here, the time-dependent field envelopes of the incident pulses and of the coherent anti-Stokes field are assumed to be identical for each point within the focal volume.

When electronic dephasing is much faster than either the nuclear dynamics of the molecular system or the optical pulses, the time-resolved CARS signal can be written as,[14]

$$S(\tau) \propto \int_{-\infty}^{\infty} dt |\mathbf{P}^{(3)}(\tau,t)|^2, \tag{1}$$

where

$$\mathbf{P}^{(3)}(\tau,t) = -E_{P2}(t) \int_0^{\infty} dt_2 E_{P1}(t+\tau-t_2) E_S^*(t+\tau-t_2)$$

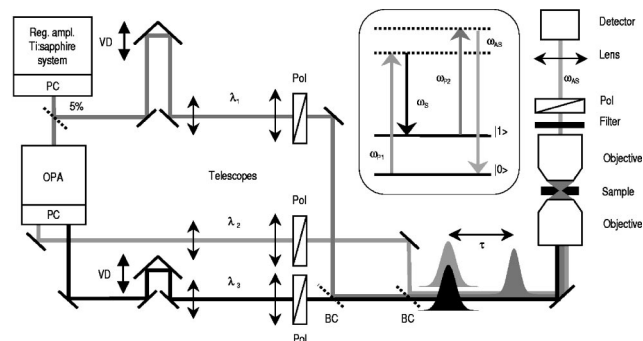$$\times \exp[i(\omega_{P1} - \omega_S)t_2]\alpha(t_2). \tag{2}$$

FIG. 1. Schematic of the time-resolved CARS microscope. Insert: Energy diagram of the four-wave mixing process with three incident fields. PC, pulse compression stage; VD, variable delay line; Pol, polarizer; and BC, dichroic beam combiner.

[a]Present address: 3. Physikalisches Institut, Universität Stuttgart, Pfaffenwaldring 57, 70550 Stuttgart, Germany.
[b]Present address: BlueLeaf Networks, Sunnyvale, CA 94085.
[c]Electronic mail: xie@chemistry.harvard.edu

The T-CARS experiment probes the correlation function of the linear polarizability response, $\alpha(t_2)$, of the sample, which in the case of parallel polarization of the three incident and the anti-Stokes fields takes the following form:[15–17]

$$\alpha(t_2,\Theta,\Phi,\Psi) = A_{nr}\delta(t_2) + \sum_l A_l^{aniso}\exp(-200i\pi c\tilde{\nu}_l t_2)$$

$$\times\left\{\left(\rho_l^{-1} - \frac{4}{3}\right)\exp(-t_2/T_{2l})\right.$$

$$\left.+ \frac{4}{3}\exp[-t_2(T_{2l}^{-1} + T_{or,l}^{-1})]\right\}. \qquad (3)$$

Here, the delta function (scaled by A_{nr}) represents the nonresonant (electronic) response of the system while the l Raman-active vibrational modes are modeled as damped exponentials of amplitude A_l^{aniso}, center wavenumber $\tilde{\nu}_l = 10^{-2}\omega_l/2\pi c$ (in cm^{-1}), vibrational dephasing time T_{2l}, rotational correlation time $T_{or,l}$, and depolarization ratio ρ_l. These parameters can be independently obtained by recording the corresponding spontaneous polarization-controlled Raman spectra of the sample, $\tilde{\alpha}^\parallel(\tilde{\nu})$ and $\tilde{\alpha}^\perp(\tilde{\nu})$, by computing their isotropic and anisotropic components, $\tilde{\alpha}^{iso}(\tilde{\nu}) = \tilde{\alpha}^\parallel(\tilde{\nu}) - \frac{4}{3}\tilde{\alpha}^\perp(\tilde{\nu})$ and $\tilde{\alpha}^{aniso}(\tilde{\nu}) = \tilde{\alpha}^\perp(\tilde{\nu})$, and by their subsequent decomposition into l isotropic and anisotropic Lorentzian Raman line profiles with $\tilde{w}_l^{iso} = 10^{-2}/\pi c T_{2,l}$ and $\tilde{w}_l^{aniso} = (T_{2l}^{-1} + T_{or,l}^{-1})/100\pi c T_{2l}$ being the full width of half maximum [(FWHM) in cm^{-1}] values, respectively.

Numerical simulation of the T-CARS measurement is carried out using Eqs. (1)–(3). The only parameter that is varied is A_{nr}. The time-dependent field envelopes of the incident laser pulses are assumed to be Gaussians, $E_m(t) = \exp(-2\ln 2 t^2/(\Delta_m)^2)$. The FWHM of the laser pulses, Δ_m, the laser pulse center wavenumbers, $\tilde{\nu}_m$, and the spontaneous polarization Raman spectrum of the sample are obtained from independent experiments.

The experimental layout of the RFID microscope is schematically depicted in Fig. 1. A regeneratively amplified Ti:Sapphire laser system that pumps an optical parametric amplifier (OPA) [RegA 9000/OPA, 9400, Coherent Inc.] at a repetition rate of 250 kHz was used to provide synchronized femtosecond pulse trains at three different wavelengths that are given by the fundamental (λ_1) of the Ti:Sapphire, the signal (λ_2), and the idler (λ_3) output of the OPA. The different frequencies of the probe and pump beams avoids the interference between the two beams in the colinear geometry. Before being focused, all fields were independently expanded to a beam diameter that matches the back aperture of the objective lens (Nikon Plan Apo oil, 60× NA = 1.4) linearly polarized along the x axis, collinearly overlapped, and coupled into an inverted optical microscope (Nikon TE 300). The FWHM values of the laser pulses were Δ_1 = 185 fs, Δ_2 = 85 fs, and Δ_3 = 115 fs as obtained by intensity autocorrelation measurements, with corresponding transform limited spectral band widths of 80, 173, and 128 cm^{-1}, respectively. Two variable optical delay lines were used to control the temporal overlap and delay between the different pulse trains. The anti-Stokes signal was parfocally collected with an identical objective lens in the forward direction, spectrally isolated using interference band pass and holographic notch
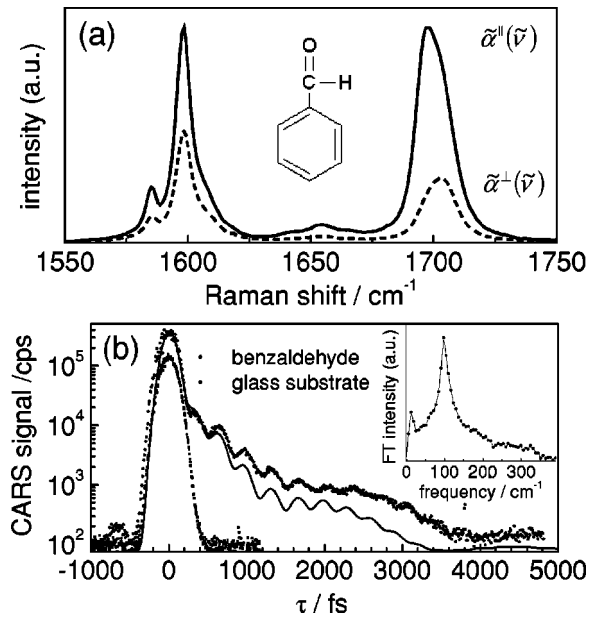

FIG. 2. Information content of RFID measurements demonstrated for neat benzaldehyde. (a) Parallel [$\tilde{\alpha}^\parallel(\tilde{\nu})$, solid line] and perpendicular [$\tilde{\alpha}^\perp(\tilde{\nu})$, dashed line] components of the spontaneous Raman spectrum with respect to the linear polarized orientation of the incident field; (b) Measured (circles) and simulated (line) RFID decay curves. The instrumental response function measured solely from the nonresonant coherent radiation originating from the glass substrate is also shown (squares). Insert: Fourier transform of the oscillatory contributions to the measured RFID. ($\lambda_{P1} = \lambda_1 = 800.1$ nm, $\lambda_S = \lambda_3 = 920.5$ nm, $\lambda_{P2} = \lambda_2 = 715.6$ nm, corresponding to a Raman shift centered at 1636 cm^{-1} with average powers of each ~50 μW).

filters, passed through an analyzing polarizer, and detected by an avalanche photodiode (SPCM-AQR15, EG&G Canada). Images were collected by raster scanning the sample, respective to the fixed laser beams.

To demonstrate the ability of the T-CARS microscope to record RFID, measurements on neat benzaldehyde have been performed. Figure 2(a) displays the parallel and perpendicular polarized spontaneous Raman spectrum with respect to the linear polarized incident field, which was taken with a commercial confocal Raman microscope (LabRam, Dilor). The Raman bands at 1585 and 1598 cm^{-1} are assigned to the two quadrant stretch components of C=C bonds in the benzene ring, whereas the 1700 cm^{-1} band reflects the nonconjugated C=O stretch vibration.[18] Their depolarization ratios amount to 0.43, 0.53 and 0.33, respectively. Figure 2(b) displays the RFID measurement of benzaldehyde when tuned to a Raman shift centered at 1636 cm^{-1}. Due to the broad spectral width of the pump and Stokes fields, the superposition of all three vibrational resonances, shown in Fig. 2(a), are coherently excited and contribute to the measured RFID of benzaldehyde. An initial fast decay that follows the instrumental response, a multi-exponential decay, and superimposed quantum beats with period times at ~340 fs and ~2500 fs are observed. The Fourier transform of the oscillatory contributions to the measured decay curve into the frequency domain [see inset in Fig. 2(b)] reveals two distinct difference frequencies at 13 and 97 cm^{-1}, which can be assigned to the beating of the 1598 cm^{-1} mode with the 1585 cm^{-1} and 1700 cm^{-1} mode, respectively. The numerical simulation of RFID is also depicted in Fig. 2(b), satisfac-

Appl. Phys. Lett., Vol. 80, No. 9, 4 March 2002

Volkmer, Book, and Xie   1507

torily reproducing the characteristic features of the observed decay curve. The temporal resolution of the T-CARS microscope is given by the instrumental response function (IRF) that has been independently measured by detecting the solely nonresonant coherent radiation originating from the glass substrate. The FWHM of the IRF amounts to 200 fs.

Next, we apply the technique to demonstrate vibrational imaging of a 1-μm diameter polystyrene bead that is embedded in water. First, the spontaneous Raman depolarization spectra were taken, with the parallel spectrum shown in the inset of Fig. 3(a). The spectrum is decomposed into a series of Lorentzian line profiles, which correspond to the aromatic CH stretching modes of the benzene ring at 3035, 3051, and 3061 cm^{-1}.[18] Figure 3(a) reveals the RFID when focused into the bead and tuned to a Raman shift centered at 3054 cm^{-1}, and therefore coherently exciting all the vibrational modes shown in the inset of Fig. 3(a). The measured RFID curve exhibits an initial fast decay of the IRF, followed by a single exponential decay with a time constant of about ~390 fs, which is superimposed with a quantum beat that recurs at $\tau \approx 1280$ fs. The fastest feature in the time domain, the decay constant of 390 fs, corresponds to the broadest feature in the frequency domain, the line width (FWHM $= 15.4$ cm^{-1}) of the 3035 cm^{-1} resonance, which gives $T_2/2 \approx 345$ fs and appears to be the dominant contribution to the observed RFID curve. The beating of the 3035 cm^{-1} mode with the 3061 cm^{-1} mode with a difference frequency of 26 cm^{-1} accounts for the observed quantum beat period of ~1280 fs. More quantitatively, the numerical simulation [Fig. 3(a)] satisfactorily reproduces the experimental data.

Repeating this experiment in bulk water results in a decay curve that solely resembles the IRF. This indicates that the observed signal arises purely from the nonresonant and/or spectrally very broad resonance contributions of water in the 3000–3100 cm^{-1} range. Figure 3(b) displays ultrafast vibrational images of a polystyrene bead at zero-time delay and at $\tau = 484$ fs. Comparison of the two images clearly reveals that the time-delayed detection is capable of completely removing the nonresonant background contributions. As such, the solvent background signal is suppressed by a factor of ~570, with the remaining background signal in the time-delayed image being limited by the dark count level of the detection system only. In contrast, the maximum signal from the polystyrene bead at time zero is reduced by only a factor of 50. Consequently, the signal-to-background ratio, S/B, increases from $S/B(\tau=0) \approx 3$ to $S/B(\tau=484\ \text{fs}) \approx 35$. In this way, the vibrational contrast in the time-delayed image arises exclusively from the Raman-resonant modes. The lack of interference with any nonresonant signal allows one to quantitatively relate the recorded image pixel intensity to the squared concentration of the vibrational modes within the sample.

In conclusion, the T-CARS microscope is capable of completely removing nonresonant background signal from the sample and the solvent, and thus significantly increases the detection sensitivity of coherent Raman microscopy. Time-domain experiments on vibrational imaging are complimentary to their analogous frequency domain experiments of chemical and biological systems.
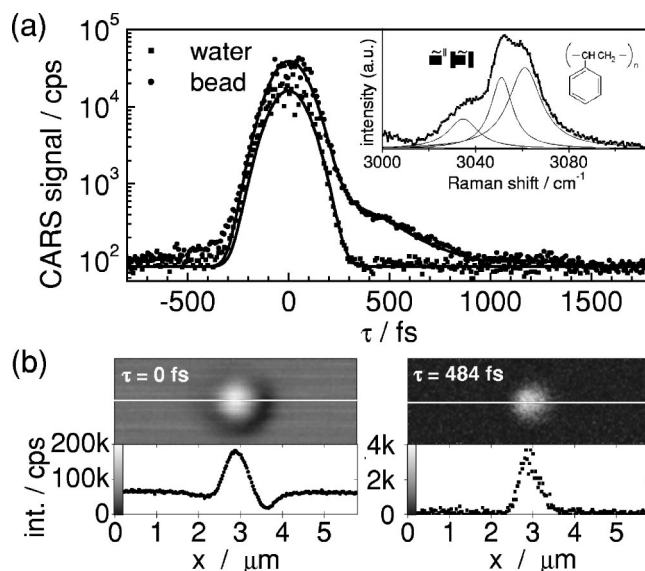
The authors thank Professor R. M. Hochstrasser for

FIG. 3. Temporally and spatially resolved CARS signals from a 1-μm diameter polystyrene bead embedded in water. (a) Measured and simulated (line) decay curves when focused on the bead (circles) and into bulk water (squares), and the parallel component of the spontaneous Raman spectra with its decomposition into Lorentzian line profiles (inset); (b) RFID images and the lateral intensity profiles along the white line at time zero and at $\tau \approx 484$ fs, demonstrating the complete removal of non-resonant background contributions from the sample and solvent to the image contrast in the latter. The image size amounts to 200×70 (pixel)^2 with an integration time of 4.88 ms per pixel. ($\lambda_{P1}=\lambda_1=714.6$ nm, $\lambda_{P2}=\lambda_2=798.1$ nm, $\lambda_S=\lambda_3=914.1$ nm, corresponding to a Raman shift centered at 3054 cm^{-1} with average powers of each ~43 μW).

[1] J. N. Gannaway and C. J. R. Sheppard, Opt. Quantum Electron. **10**, 435 (1978).
[2] P. J. Campagnola, M. D. Wei, A. Lewis, and L. M. Loew, Biophys. J. **77**, 3341 (1999).
[3] L. Moreaux, O. Sandre, and J. Mertz, J. Opt. Soc. Am. B **17**, 1685 (2000).
[4] Y. Barad, H. Eisenberg, M. Horowitz, and Y. Silberberg, Appl. Phys. Lett. **70**, 922 (1997).
[5] M. Müller, J. Squier, K. R. Wilson, and G. J. Brakenhoff, J. Microsc. **191**, 266 (1998).
[6] A. Zumbusch, G. R. Holtom, and X. S. Xie, Phys. Rev. Lett. **82**, 4142 (1999).
[7] A. Volkmer, J.-X. Cheng, and X. S. Xie, Phys. Rev. Lett. **87**, 023901 (2001).
[8] J.-X. Cheng, A. Volkmer, L. D. Book, and X. S. Xie, J. Phys. Chem. B **105**, 1277 (2001).
[9] J.-X. Cheng, L. D. Book, and X. S. Xie, Opt. Lett. **26**, 1341 (2001).
[10] Y. R. Shen, *The Principles of Nonlinear Optics* (Wiley, New York, 1984).
[11] A. Laubereau and W. Kaiser, Rev. Mod. Phys. **50**, 607 (1978).
[12] F. M. Kamga and M. G. Sceats, Opt. Lett. **5**, 126 (1980).
[13] J.-X. Cheng, A. Volkmer, and X. S. Xie, *J. Opt. Soc. Am. B* (to be published).
[14] S. Mukamel, *Principle of Nonlinear Optical Spectroscopy* (Oxford University Press, New York, 1995).
[15] R. F. Loring and S. Mukamel, J. Chem. Phys. **83**, 2116 (1985).
[16] D. McMorrow and W. T. Lotshaw, Chem. Phys. Lett. **174**, 85 (1990).
[17] W. Li, H.-G. Purucker, and A. Laubereau, Opt. Commun. **94**, 300 (1992).
[18] D. Lin-Vien, N. B. Colthup, W. G. Fateley, and J. G. Grasselli, *The Handbook of Infrared and Raman Characteristic Frequencies of Organic Molecules* (Academic, San Diego, 1991).